Materials Advances

ROYAL SOCIETY OF CHEMISTRY

PAPER

View Article Online
View Journal | View Issue

Cite this: *Mater. Adv.*, 2026, 7, 3645

Delayed crosslinking enables ultra-high-resolution melt electrowriting of responsive liquid crystal elastomers

Mehrzad Javadzadeh, [a] María Fernández-Melero,[a] Jesús del Barrio [b] and Carlos Sánchez-Somolinos *[ac]

Melt electrowriting (MEW) enables the fabrication of finely structured scaffolds with sub-micrometer resolution. However, reducing the inter-fiber distance (IFD) in MEW remains challenging due to electrostatic interactions between the charged polymer jet and previously deposited fibers, often leading to fiber bridging. Recently, we demonstrated that MEW of reactive liquid crystalline inks, followed by ultraviolet (UV) photopolymerization, enables the fabrication of digitally positioned liquid crystal elastomer (LCE) structures. Building on this, we demonstrate that tuning the UV light intensity during photopolymerization significantly improves the achievable resolution range. Lower UV intensities produce smaller minimum IFDs without fiber bridging, enabling the fabrication of highly ordered structures with IFDs down to 11 μm for 5 μm-diameter fibers, a feature that, to the best of our knowledge, surpasses the smallest IFDs previously reported for MEW. We hypothesize that slower crosslinking kinetics extend the time window for charge dissipation, reducing electrostatic interactions between the jet and the previously deposited fibers. Although the mechanism remains unclear, local variations in material flow or curing-induced surface morphology may also affect electric field distribution. Beyond resolution improvements, this strategy enables defect-free fabrication of stimuli-responsive LCEs with programmable shape transformation and actuation. UV light intensity thus emerges as a critical design parameter for MEW, with implications for other photo-crosslinkable systems.

Received 11th October 2025,
Accepted 22nd February 2026

DOI: 10.1039/d5ma01174d

rsc.li/materials-advances

Introduction

Additive manufacturing (AM) is transforming various industries by allowing the rapid, efficient, and precise layer-by-layer production of complex structures.[1] Specifically, nozzle-based direct writing has played a key role in this transformation, expanding the range of processable materials, including polymer melts, shear-thinning hydrogels, and metallic, ceramic, or polymeric colloidal inks.[2–4] However, generating sub-100 micron fibers remains challenging with extrusion-based digital deposition technologies, mainly because of the high pressures required to extrude inks through nozzles with small diameters.

In recent years, a new method called Melt electrowriting (MEW) has been developed to address this limitation.[5] MEW establishes a high voltage between the nozzle and the collector to electrodynamically stabilize a charged polymer jet, producing a fine fiber that is precisely positioned by digitally controlling the relative movement of the printhead with respect to the substrate. Once deposited, these fibers are fixed, either by cooling-induced solidification for thermoplastic materials such as poly(ε-caprolactone) (PCL) or by post-deposition polymerization and network formation in solvent-free reactive systems.[6–9] Additionally, the electrostatic attraction enables precise fiber stacking, resulting in well-defined, high walls. MEW has thus demonstrated a remarkable ability to produce micron- and submicron fibers,[10] as well as digitally defined structures with geometrical features that far exceed the resolution limits of scaffolds produced by conventional extrusion-based AM techniques.[6–9]

Like other AM techniques, MEW is constrained by resolution limitations. In electrohydrodynamic (EHD) techniques like MEW, surface charge accumulation of deposited fibers can cause electrostatic instabilities, undermining deposition accuracy and limiting the achievable resolution.[11] If the previously deposited fibers cannot dissipate their residual charge

[a] *Instituto de Nanociencia y Materiales de Aragón (INMA), CSIC-Universidad de Zaragoza, Departamento de Física de la Materia Condensada, Zaragoza, 50009, Spain. E-mail: carlos.s@csic.es*
[b] *Instituto de Nanociencia y Materiales de Aragón (INMA), CSIC-Universidad de Zaragoza, Departamento de Química Orgánica, Zaragoza, 50009, Spain*
[c] *Centro de Investigación Biomédica en Red de Bioingeniería, Biomateriales y Nanomedicina (CIBER-BBN), Instituto de Salud Carlos III, Madrid 28029, Spain*

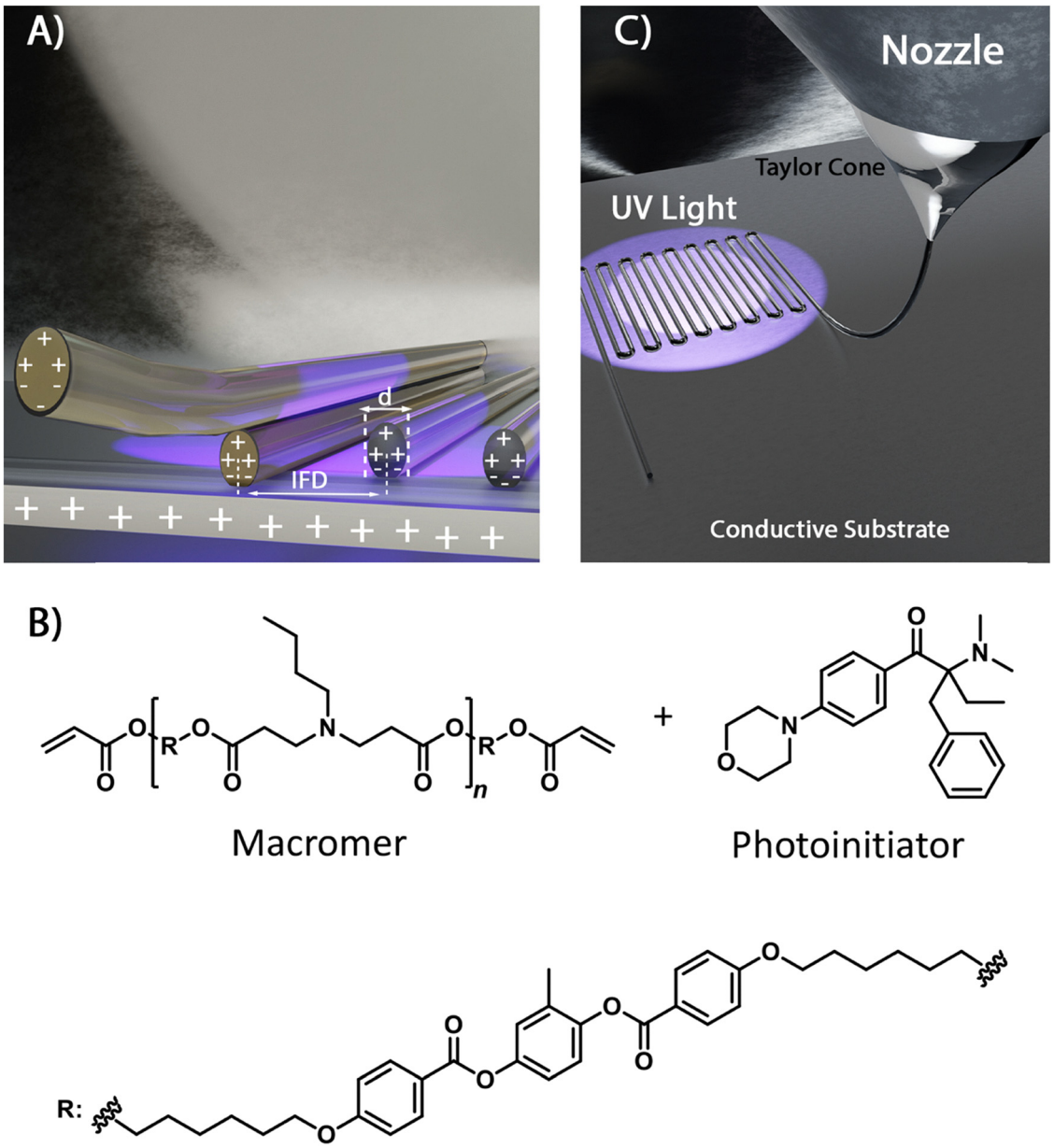

Fig. 1 MEW of LCE. (A) Conceptual illustration of charge distribution in a deposited and incoming fiber on a conductive substrate electrically connected to the collector. The figure highlights key geometrical parameters: the diameter of the deposited fiber and the interfiber distance (IFD). (B) Chemical structures of the ink components. (C) Schematic representation of the MEW and UV curing process, including the nozzle and Taylor cone for fiber formation, a conductive substrate for charge dissipation, and UV light irradiation used to crosslink the deposited fibers.

effectively, this can lead to electrostatic field distortions that can deflect the incoming fiber from its intended path. As electrostatic interactions between the depositing and previously deposited fibers become stronger at short distances, this effect is particularly pronounced when two parallel fibers are written in close proximity, as illustrated in Fig. 1A. This can lead to an inaccurate fiber placement phenomenon known as "fiber bridging". In this situation, the new depositing fiber is drawn towards the previously placed one, deviating from the intended printing path. This fiber bridging is the primary challenge in creating small-period scaffolds using MEW.[9,11,12] Different strategies have been proposed to mitigate electrostatic instabilities in MEW by enhancing charge dissipation from deposited fibers. Some studies have shown that conductive substrates can reduce these instabilities by facilitating charge dissipation from previously deposited fibers.[11,12] Also, Cao and coworkers carried out MEW of PCL, varying the collector temperature from 16 °C to 30 °C. Although collector temperature can influence the charge distribution, the extent of polarization in the processed material, and the residual charge amount, their studies concluded that these aspects have a limited influence on preventing fiber bridging when printing single parallel fibers at small interfiber distances (IFDs).[13] As a result, the generation of well-defined scaffolds composed of

parallel lines with small IFDs on the order of a few tens of microns remains challenging.[14] Recent work by Du and Xu has systematically investigated these resolution limits in thermoplastic melt electrowriting, reporting IFDs down to approximately 25 μm for PCL scaffolds through careful optimization of printing kinematics and process parameters.[15] Related solution-based electrohydrodynamic printing studies, which are not strictly MEW, have suggested that collector design and charge dissipation can influence achievable fiber spacing.[16] Moreover, as the number of printed layers increases, precise deposition becomes increasingly complex due to cumulative electrostatic interactions and field distortions induced by the growing, potentially charged structure, raising the minimum achievable IFD without fiber bridging. In contrast to these approaches, which primarily rely on optimization of printing kinematics, collector design, or process parameters in thermoplastic or solution-based systems, the present work explores a complementary strategy based on tuning curing kinetics in reactive, solvent-free MEW systems.

Recently, we have presented the melt electrowriting of reactive liquid crystalline inks, which are deposited as solvent-free viscoelastic melts and subsequently stabilized by ultraviolet (UV) photopolymerization, leading to digitally positioned liquid crystal elastomer (LCE) fibers with diameters ranging from hundreds of nanometers to tens of micrometers. This process results in well-defined stack walls composed of ultra-fine LCE fibers. Moreover, the electrowriting process induces a preferential alignment of the mesogenic constituent molecules of the ink along an orientation direction, defined by the director n, which lies parallel to the fiber axis. In LCEs, large and reversible anisotropic shape changes take place in response to certain external stimuli. An increase in temperature, for example, induces a decrease in the mesogenic order, leading to a contraction of the LCE along the director and a simultaneous expansion perpendicular to it. Advantageously, since the molecular alignment is determined by the MEW printing path, a precise digital control of the mechanical response of the printed LCE upon stimulation can be achieved.[17]

In our previous work, we explored the preparation of small period structures, obtaining 90 μm period square lattice scaffolds of 5 layers per wall with no defects.[17] When exploring smaller periods, fiber bridging between adjacent scaffold lines often occurred, resulting in structural defects, providing an idea of the current resolution limits of MEW when applied to these liquid crystalline materials.

As managing residual charge on deposited fibers plays a critical role in fiber-to-fiber interactions and influences deposition accuracy, the active control of charge dissipation during or after deposition could provide new pathways to push resolution limits. It is well known that polymer crosslinking leads to increased rigidity and density of the material, limiting the mobility of charge carriers. Macroscopically, this crosslinking results in a significant decrease in the electrical conductivity of the material.[18] We hypothesize that by modifying the curing process of the deposited fibers, specifically by varying the ultraviolet (UV) light curing intensity during LCE photopolymerization, we could influence network characteristics that affect the ability to manage residual electrostatic effects, thus impacting the minimum achievable IFD without bridging. Based on this assumption, in this work, we systematically investigated how UV curing intensity affects the resolution limits of MEW for reactive LCE inks. We explored this for different fiber diameters and different numbers of layers. By tuning the polymer network formation process through photocuring, our goal is to push the resolution limits of MEW and enable the fabrication of highly ordered, fine-featured, stimuli-responsive systems.

Results and discussions

To experimentally evaluate our hypothesis, we systematically explored the effect of UV light intensity during photopolymerization on the resolution limits of MEW in LCE systems. Our study focuses on quantifying the minimum IFD achievable without fiber bridging across various fiber diameters and scaffold heights. The following sections detail the ink preparation, MEW methodology, and key findings regarding how curing conditions can enhance printing precision and enable the fabrication of ultra-fine, anisotropic LCE scaffolds with thermally responsive behavior.

Ink preparation

As ink, we used an acrylate-functionalized main-chain liquid crystal polymer with a UV-sensitive photoinitiator, Irgacure 369 (Fig. 1B). The synthesis of the reactive macromer was done following a previously reported procedure, which employs the Aza-Michael addition reaction of *n*-butylamine with a mesogenic diacrylate, C6M.[17] To carry out this addition reaction, the amine and the diacrylate monomer are added to an amber flask to protect against undesired UV-photoinduced curing in a molar ratio of 1 : 1.3. The excess of C6M ensures that the polymer chains terminate with acrylate groups, resulting in a macromer that can later be photo-crosslinked, ultimately forming the final LCE material.[17,19] Such a stoichiometric imbalance is required to achieve a sufficiently high degree of crosslinking within the system, resulting in stiff materials that enable thin walls prepared by MEW to remain vertical without bending or collapsing (*vide infra*).

Electrowriting of parallel fibers with small interfiber distances: resolution limit determination

Electrowriting was carried out using a GeSIM Bio-Scaffolder 3.2, equipped with an integrated electrowriting module. This system features a temperature-regulated printhead with controlled *X*–*Y*–*Z* movement and a static collector. The electric field is generated by applying a positive voltage to the collector and grounding the nozzle. The gap between the nozzle and collector was precisely maintained at 2 mm above the printing area (see Experimental section) while the printhead temperature was kept at 25 °C. The fine selection of MEW parameters, such as

voltage, printhead pressure, and velocity, is crucial for achieving precise fiber deposition to form well-defined scaffolds.[20,21] The nozzle orifice diameter, 100 μm in our case, also directly influences the diameter of the deposited fiber.[17,21,22] We used a glass substrate with an indium tin oxide (ITO) coating, which was electrically connected to the collector. Conductive ITO substrates facilitate charge dissipation from deposited fibers to ground and stabilize the local electric field at the collector surface, thereby improving fiber placement fidelity during melt electrowriting, as previously reported in the literature.[11] Once the fiber is deposited, a UV lamp above the collector irradiates the deposited material and initiates photo-crosslinking, forming the LCE (Fig. 1C). Because the UV irradiation wavelength range employed (320–390 nm) corresponds to the absorption range of the photoinitiator (Irgacure 369), while the liquid crystalline mesogenic units do not exhibit significant absorption at these wavelengths, the applied UV light selectively initiates photopolymerization rather than directly exciting the mesogenic moieties.

In our previous work, we introduced MEW as a method to produce well-defined shapes and scaffolds of LCEs. However, as mentioned in the introduction, achieving high-layered scaffolds with periods below 90 μm proved challenging.[17] To explore the MEW resolution limit, in the current work, we printed parallel fibers following the methodology proposed by Dalton and coworkers.[11] In this approach, fibers are deposited in parallel with systematically varied IFDs. As already described in the introduction, for sufficiently large IFD, the incoming fiber does not interact significantly with the previously deposited one, and thus, the first gets attracted to the substrate following the printing path as programmed. However, as the IFD is progressively reduced, a critical distance is reached, referred to as the minimum IFD without fiber bridging, below which the electrostatic attraction from the previously deposited fiber becomes strong enough to deflect the incoming fiber, resulting in fiber bridging. This phenomenon marks the onset of fiber bridging and defines the resolution limit in terms of the minimum achievable IFD. The minimum IFD corresponds to the smallest programmed spacing at which fibers could be deposited reproducibly along the intended printing path without lateral deflection or loss of positional fidelity. This threshold was determined by systematically reducing the target IFD in successive printing experiments until deposition defects consistently appeared. Scanning electron microscopy was used to analyze both successful and unsuccessful deposition attempts to establish this limit.

We initially studied the resolution limits when printing parallel fibers with a target diameter of 5 μm (Fig. 2 and Fig. S1 of the SI).

Once the appropriate combination of printing parameters (pressure, speed, and voltage) was established to generate this fiber diameter consistently, these parameters were maintained constant throughout the different printing experiments focused on this specific fiber diameter. After the initial stabilization of the jet, sets of parallel fibers were electrowritten with progressively decreasing IFDs to determine the minimum IFD without fiber bridging. In the first set of experiments, a UV light intensity of 15 mW cm^{-2}, hereafter referred to as high UV light intensity, was used to cure the deposited fibers. As demonstrated in our previous work, this light intensity effectively crosslinks the ink into an LCE, leading to well-defined fibers that stack layer by layer.

Fig. 2A–C show scanning electron microscope (SEM) images of samples printed at the minimum IFD without fiber bridging, with different numbers of layers, using 15 mW cm^{-2} of UV light intensity for curing. For one layer (1L in Fig. 2A), the minimum

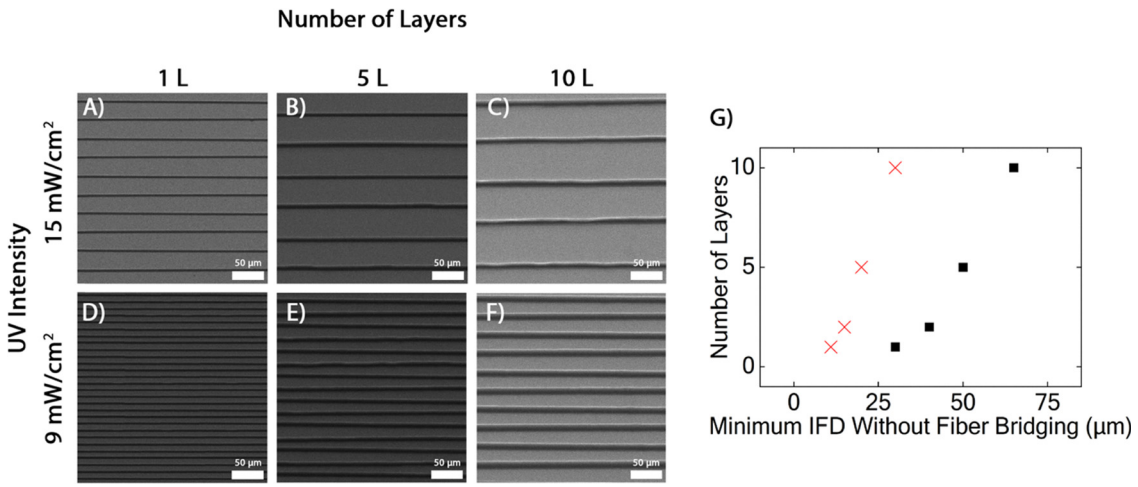

Fig. 2 Effect of UV light intensity and number of layers on the minimum IFD without Fiber Bridging for 5 μm-diameter fibers. (A–C) SEM images of melt electrowritten (MEW) fibers deposited under high UV light intensity (15 mW cm^{-2}) showing the minimum IFD at which no fiber bridging occurred for (A) 1 layer (1L), (B) 5 layers (5L), and (C) 10 layers (10L). (D–F) SEM images of samples printed under low UV light intensity (9 mW cm^{-2}), also showing the minimum IFD without fiber bridging for (D) 1 layer (1L), (E) 5 layers (5L), and (F) 10 layers (10L). (G) Plot showing the relationship between minimum IFD without fiber bridging and the number of deposited layers for 5 μm-diameter fibers. Red crosses correspond to experiments conducted under low UV light intensity conditions, and black squares indicate high UV light intensity. The standard deviation (SD) of the measured IFDs was 1.85 μm (A), 3.01 μm (B), 4.76 μm (C), 0.51 μm (D), 3.49 μm (E), and 1.77 μm (F), based on 10 measurements per condition. Scale bars: 50 μm.

IFD without bridging was 30 μm. Fiber bridging was observed when printing lower IFDs, such as 25 μm (see Fig. S2 in the SI). As the number of layers increased, the minimum interfiber distance without bridging also increased, reaching 50 μm for five layers (5L, Fig. 2B) and 65 μm, as shown in Fig. 2C, for ten layers (10L, Fig. 2C).

Next, we carried out a similar set of experiments to determine the minimum IFD without bridging, using, this time, a lower UV irradiation intensity of 9 mW cm^{-2} for curing (40% lower than in the previous experiment), hereafter referred to as low UV light intensity, while keeping all other printing parameters constant. Photopolymerization using lower UV light intensity levels (*e.g.*, 8 mW cm^{-2}) resulted in insufficient curing, causing the deposited fibers to fuse into thicker filaments rather than forming well-defined walls and structures (see Fig. S3 in the SI). Fig. 2D–F show SEM images of samples printed at the minimum IFD without fiber bridging for the different numbers of layers, all of them cured with 9 mW cm^{-2} of UV light. In this case, the minimum interfiber distance without bridging was 11 μm for a single layer (1L, Fig. 2D), almost three times smaller than that obtained under higher UV intensity (Fig. 2A).

Fiber bridging was observed at 10 μm for a one-layer sample (see Fig. S4 in the SI). As the number of layers increased, the minimum IFD without bridging also increased, reaching a value of 20 μm for five layers (5L, Fig. 2E) and 30 μm for ten layers (10L, Fig. 2F). Notably, in multilayered samples, especially under low UV light intensity, the resulting walls appear thicker than the nominal 5 μm fiber diameter. This is likely due to delayed solidification, allowing partial flow or spreading of the deposited material before complete crosslinking. The lower curing intensity may prolong the viscous state of the deposited fibers, promoting fusion between layers and giving rise to broader fiber and wall features in SEM.

Fig. 2G summarizes the minimum IFD without fiber bridging for printed parallel fibers with a different number of layers and under the two UV light intensity conditions. The reported standard deviations (SDs) reflect local interfiber spacing variability within successfully printed regions and therefore quantify placement precision. Consistently, for each fixed UV light intensity, the minimum IFD without bridging progressively increases with the number of layers, as previously reported by Dalton *et al.* for poly(ε-caprolactone) melt-electrowritten fibers.[11] Remarkably, in experiments conducted at low UV light intensity, the minimum IFDs without fiber bridging were significantly smaller across different numbers of layers compared to those performed under high UV light intensity. At very small IFDs, residual charge accumulation on previously deposited fibers causes strong electrostatic interactions and local electric-field distortions that deflect the incoming jet. These effects intensify with increasing layer number due to cumulative charge buildup and geometric confinement, thereby defining the practical resolution limit.

We further explored the resolution limits under different UV light intensity conditions for fibers with diameters as small as 2 μm. Fig. 3 (and Fig. S5 of the SI) presents SEM images of samples printed at the minimum IFD without fiber bridging for different numbers of layers, using UV light intensities of 15 mW cm^{-2} and 9 mW cm^{-2} for curing. As shown in Fig. 3G, the trends observed in the minimum IFD without bridging for 2 μm fibers are qualitatively consistent with those observed for 5 μm fibers (Fig. 2G). For a given curing condition,

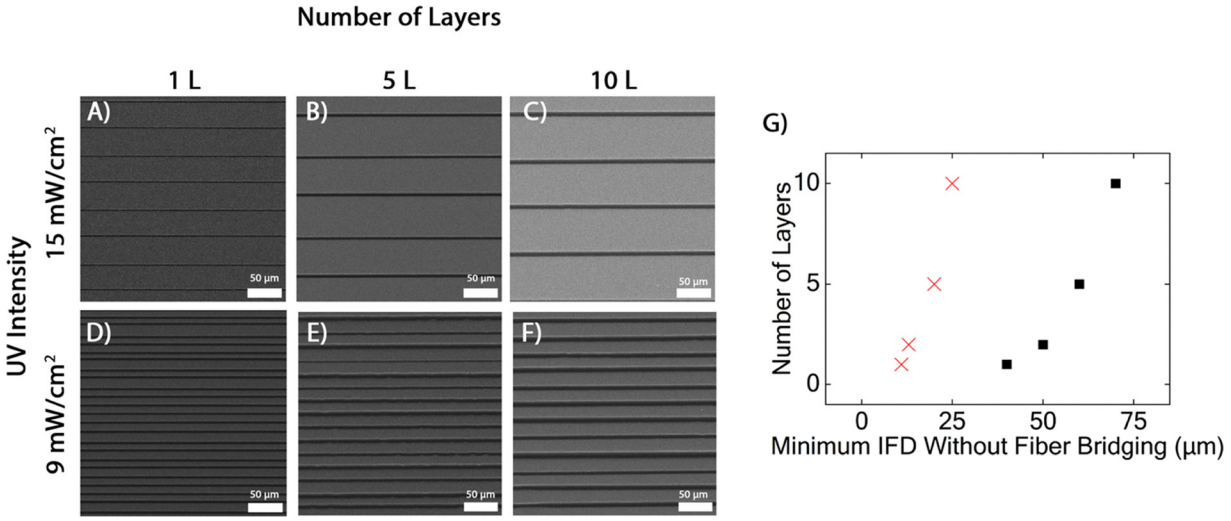

Fig. 3 Effect of UV light intensity and number of layers on the minimum IFD without fiber bridging for 2 μm-diameter fibers. (A)–(C) SEM images of melt electrowritten (MEW) fibers deposited under high UV light intensity (15 mW cm^{-2}) showing the minimum IFD at which no fiber bridging occurred for (A) 1 layer (1L), (B) 5 layers (5L), and (C) 10 layers (10L). (D–F) SEM images of samples printed under low UV light intensity (9 mW cm^{-2}), also showing the minimum IFD without fiber bridging for (D) 1 layer (1L), (E) 5 layers (5L), and (F) 10 layers (10L). (G) Plot showing the relationship between minimum IFD without fiber bridging and the number of deposited layers for 5 μm-diameter fibers. Red crosses correspond to experiments conducted under low UV light intensity conditions, and black squares indicate high UV light intensity. The SD of the interfiber spacing was 2.38 μm (A), 4.20 μm (B), 2.41 μm (C), 1.90 μm (D), 1.16 μm (E), and 2.15 μm (F), calculated from 10 SEM-based measurements. Scale bars: 50 μm.

smaller minimum IFDs without bridging were achieved at a lower number of layers. Furthermore, similar to results from the 5 μm fiber experiments, significantly smaller minimum IFDs without bridging were obtained for all the numbers of layers when a lower UV curing intensity was used. Finally, when quantitatively comparing the minimum IFD without fiber bridging between the two fiber diameters (Fig. 2G and 3G), the 2 μm fibers showed a slightly better resolution performance. This observation is consistent with previous findings in PCL reported by Dalton and coworkers.[11]

As noted earlier, polymer crosslinking increases the rigidity and density of the material, restricting charge carrier mobility.[23,24] We tentatively ascribe the improved resolution observed under lower UV light intensity to the delayed crosslinking kinetics, which may provide a longer time window for residual charges to dissipate before the polymer network solidifies. This enhanced charge relaxation likely reduces electrostatic interactions between the jet and the previously deposited fibers, thereby mitigating fiber deflection, bridging, and ultimately improving resolution.

To further assess the influence of UV light intensity on crosslinking kinetics, Fourier transform infrared (FTIR) spectroscopy was used to monitor acrylate conversion in the reactive ink. FTIR spectra of the uncured ink and samples irradiated for 60 s at 9 mW cm^{-2} and 15 mW cm^{-2} reveal a progressive decrease in the acrylate band at approximately 810 cm^{-1} with increasing UV intensity (Fig. S6, SI). This trend indicates a higher degree of acrylate conversion at higher irradiation intensity, confirming that reduced UV intensity leads to slower network formation at fixed exposure time. These observations support the proposed mechanism in which delayed crosslinking kinetics extend the time window for charge dissipation during MEW.

Electrowriting of square lattice LCE structures with small interfiber distances: resolution limit determination

To further advance the development of functional scaffold-type structures, we investigated the formation of square lattice scaffolds with small periodicities, taking advantage of our enhanced resolution capabilities achieved under optimized photopolymerization conditions. While depositing parallel fibers with close interfiber distance is inherently challenging, creating square lattices introduces additional complexity. Unlike unidirectional parallel fiber deposition, where electrostatic interactions are limited to fibers aligned in the same direction, square lattice formation involves interactions between fibers parallel and perpendicular to each other. At the intersection points, where fibers are deposited on each other, local material accumulation occurs, resulting in elevated features that further perturb the surrounding electrostatic environment. These local field distortions can lead to fiber deposition inaccuracies, including fiber bridging, misalignment, and deviation from the programmed printing path, making the fabrication process of these scaffold-type structures significantly more intricate.[25]

For structures with sufficiently large periodicities, on the order of several hundred micrometers, electrostatic interactions between the incoming fiber and previously deposited layers are minimal. This reduced interaction allows for accurate fiber positioning, resulting in vertical walls with a well-defined square lattice geometry and clearly shaped, uniform square pores. This behavior is also observed in our LCE materials, as shown in Fig. 4A, which presents a square lattice scaffold with a period of 300 μm, consisting of 25 layers per wall (resulting in 50 intersections), fabricated with 5 μm diameter fiber, under a low UV light intensity of 9 mW cm^{-2}.

During printing, the MEW fibers stack and fuse, leading to continuous walls with a height of about 170 μm and a smooth surface, a morphological aspect that we will comment on further below.

A closer examination of the walls forming the structure shows that the initial fibers in direct contact with the substrate define a straight vertical wall in its lower part. However, as the number of layers increases, the upper part of the thin walls becomes more prone to buckling or collapsing near the center, while the junctions at fiber intersections remain vertical. From our observations, such a trend is more pronounced in higher and longer walls, especially when the wall thickness is small in relation to its height and length.

Conversely, when printing square lattice structures with smaller periods, electrostatic interactions between the incoming fibers and the pre-deposited layers become increasingly

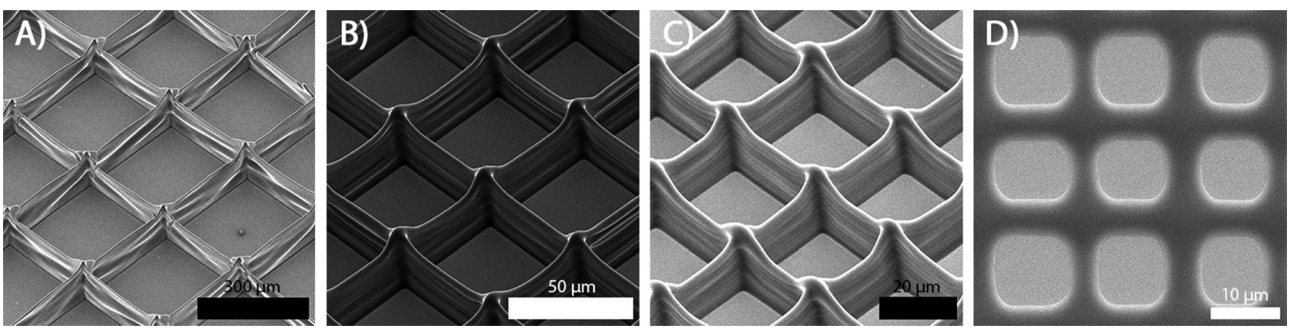

Fig. 4 MEW of square lattice LCE structures using low UV light intensity. SEM images of structures prepared under low UV light intensity of 9 mW cm^{-2}. (A) 5 μm fiber diameter, 300 μm period, 50 layers (scale bar: 300 μm); (B) 2 μm fiber diameter, 50 μm period, 32 layers (scale bar: 50 μm); (C) 2 μm fiber diameter, 30 μm period, 20 layers (scale bar: 20 μm); (D) 2 μm fiber diameter, 15 μm period, 4 layers (scale bar: 10 μm).

significant, often resulting in fiber misalignment and structural defects. Nevertheless, by leveraging the resolution enhancement provided by curing with low UV light intensity, we have successfully fabricated defect-free square lattice LCE structures with periods in the tens of microns, something not achieved using high UV light intensity. Fig. 4B–D show examples of square lattice structures with periods of 50 μm, 30 μm, and 15 μm, respectively, and composed of 32 (16 + 16), 20 (10 + 10), and 4 (2 + 2) layers, respectively. These structures exhibit well-defined and precisely positioned fibers, forming straight, uniform walls with a thickness of approximately 6 μm and exhibiting minimal visible defects. As with the parallel fiber walls, decreasing the lattice period makes it progressively more challenging to add additional layers due to a stronger, increasingly complex electrostatic environment and higher structural confinement.

As mentioned, another intriguing morphological aspect of these structures, cured under this lower UV light intensity, is the smooth surface of the walls made of fused fibers. This smoother morphology occurs because of the additional time allowed between fiber deposition and network gelation when curing with low UV light intensity. The material can flow slightly before crosslinking, creating a more level surface. In contrast, curing with high UV light intensity induces rapid gelation, which locks the network before significant flow occurs, resulting in a well-defined stacked fiber structure (Fig. S7). Interestingly, this phenomenology reminds the observations reported by Dalton and co-workers during thermoplastic MEW of polypropylene, where increasing the collector temperature led to smoother or even molten fiber morphologies due to reduced cooling and extended fiber fluidity of the polymer at the collector surface.[21] However, while in their case this effect arises from thermal control, in our system, it is achieved through the modulation of the curing kinetics of the reactive ink.

Anisotropy and thermally induced actuation of high-resolution LCE scaffolds

Once we established the structural characteristics of small-scale scaffolds printed under low UV light intensity conditions, we investigated their anisotropy and mechanical response. Fig. 5 presents a square lattice LCE structure prepared under this low UV light intensity. As discussed in the introduction, LCEs can undergo significant and controlled anisotropic shape transformations when exposed to external stimuli.[22] In these systems, a reduction in mesogenic order, triggered, for instance, by an increase in temperature, results in a contraction along the director and an expansion in the perpendicular direction. To achieve greater mechanical deformation, we used a different molar ratio of components in this section for macromer preparation (1 : 1.01, amine to diacrylate), resulting in longer polymer chains and a more loosely crosslinked network after the photopolymerization step, which allows for greater deformation in response to temperature changes. Nevertheless, although smaller in magnitude, qualitatively similar thermomechanical behavior was confirmed for the 1 : 1.3 ink composition used in the previous sections, as described in Fig. S8 in the SI.

As previously noted, for high UV light intensity,[17] fibers and structures printed and cured under lower UV light intensity also exhibited anisotropic alignment, with the director oriented parallel to the fiber deposition direction. This was visualized by polarization optical microscopy (POM) in Fig. 5A. The POM images confirm the anisotropic nature of the printed fibers, with light extinction at 0° (Fig. 5A1) and transmission at 45° (Fig. 5A2) relative to the transmission direction of the first

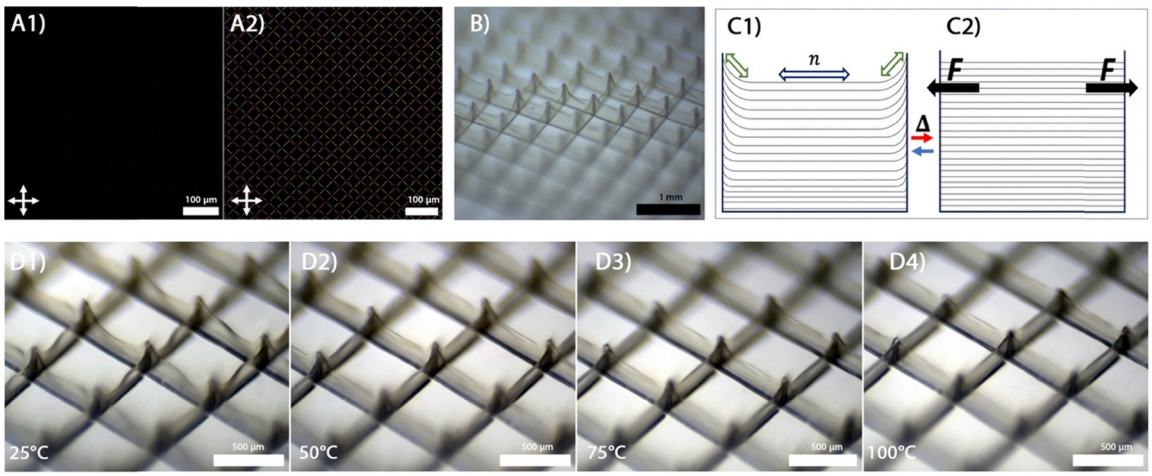

Fig. 5 Anisotropy and thermally induced actuation of square lattice LCE structures prepared under low UV light intensity. (A) Polarized optical microscopy images of a 30 μm period, 5 + 5 layered square lattice LCE structure. White arrows indicate polarizer transmission directions (scale bar: 100 μm) with the fiber direction oriented parallel (A1) and at 45° (A2) to the polarizer transmission directions. (B) Optical magnifier image of a 500 μm period square lattice composed of 50 layers (25 + 25), where fibers are uniformly stacked without forming holes or bridges, resulting in smooth walls and an optically transparent structure (scale bar: 1 mm). (C) Schematic illustration of molecular orientation (n) and contraction forces acting on the structure upon heating. (D) Optical magnifier images of a 450 μm period, 24-layer square lattice structure observed at: (D1) 25 °C, (D2) 50 °C, (D3) 75 °C, and (D4) 100 °C (scale bar: 500 μm).

polarizer, consistent with a well-defined director along the fiber axis.[17] The shear and elongational forces involved in the MEW process induce a preferential orientation of the mesogenic macromer chains along the fiber axis, which is fixed during the UV light-induced crosslinking process. These electrowritten thin walls exhibit good optical transparency, as shown in the optical magnifier image in Fig. 5B, allowing clear visualization of features behind the structure.

Despite the liquid crystalline nature of the material, this remarkable transparency suggests a uniform director alignment within the wall region, which minimizes light scattering (see Fig. S9 in the SI).

Only in the region near the fiber intersections does the director exhibit an out-of-plane component caused by the crossing fibers and subsequent material accumulation, which creates a pinnacle-like shape at the intersection.

We performed heating experiments on these samples while imaging them with an optical magnifier (Fig. 5D1–D4). At room temperature (RT), the walls tended to lose verticality, particularly in the region between two neighboring intersections if their thickness is much smaller than the height and length of the wall, as mentioned above. The partially collapsed wall straightens at 50 °C, leading to a well-defined straight box structure. To explain this result, we must consider the orientation of the director within the LCE structure. Given this orientation of the director along the length of the wall, except in the region close to the intersections of the fibers, a temperature increase leads to a contraction of the walls along the length of the forming fibers. As a result, the fibers straighten between neighboring intersections, as conceptually shown in Fig. 5C, bringing the walls to verticality. Further heating enhanced this contraction effect, resulting in nearly rectangular walls and a pronounced reduction of the pinnacle-shaped features at the intersections at 100 °C, as shown in Fig. 5D4. Heating of the structures above these temperatures led to the appearance of defects or detachment from the substrate due to excessive stretching (see Fig. S10 in the SI). For samples not subjected to this overheating process, cooling back to RT restored the initial structure, in which the walls collapsed while the intersections remained in their original position and retained their pinnacle shape. This demonstrates the reversibility of the thermally induced actuation.

Conclusions

In this work, we have demonstrated that varying the UV light intensity during the photopolymerization of reactive LCE inks in MEW can significantly influence the resolution limits of the process. By reducing the UV light intensity, we observed an apparent reduction in the minimum achievable IFD without fiber bridging. This approach enabled us to fabricate highly ordered structures with IFDs down to 11 μm, to our knowledge, below the smallest reported for MEW.

While the origin of this improvement cannot be conclusively ascribed, we hypothesize that the delayed crosslinking associated with low UV light intensity may provide additional time for the dissipation of residual charges within the deposited fibers. This extended dissipation period may reduce electrostatic interactions between the incoming jet and previously deposited fibers, thus mitigating fiber bridging and improving deposition accuracy. However, other factors might also contribute to this behavior, including differences in local material flow or surface morphology during curing, which might locally influence the electric field or influence charge transfer pathways.

Beyond pushing the resolution limits of MEW, the ability to fabricate defect-free fine LCE architectures is particularly appealing, given their intrinsic stimuli-responsive properties. The combination of high-resolution printing and programmable actuation allows the design of micro-structured systems capable of shape transformation, anisotropic motion, or mechanical reconfiguration in response to external stimuli.

Our findings establish UV light intensity during photopolymerization as a new design parameter to improve resolution in MEW of reactive materials.

Beyond the specific case of liquid crystalline elastomers studied here, the ability to control curing kinetics opens new opportunities to tune printing accuracy across a broader range of photo-crosslinkable systems. We envision that the strategy of controlling the dynamics of network formation during printing could provide a general approach for advancing the resolution limits of MEW in diverse reactive materials, an aspect that forms part of our ongoing research program.

Experimental

Materials and methods

Materials. The mesogenic diacrylate RM82, also known as C6M, was obtained from Chemfish, the chain extender *n*-butylamine was purchased from Aldrich, and the photoinitiator Irgacure 369 from Aldrich. Tetrahydrofuran (THF) from Aldrich was used as a solvent for the Michael addition reaction.

Ink preparation. The amine and mesogenic diacrylate monomers were combined in an amber container for our LCE ink formulation in the chosen stoichiometries. Molar ratios of 1 : 1.3 and 1 : 1.01 were used in this work. Irgacure 369 was added at 5 wt% as a photoinitiator. THF, equal to the total weight of the reactants, is used to dissolve the components for the Michael addition reaction, which is then allowed to proceed for one hour at 60 °C. Subsequently, the material was subjected to vacuum drying at 60 °C and 100 mbar for 48 hours to ensure complete solvent removal while removing bubbles.

MEW device configuration. Melt electrowriting was carried out using a GeSiM Bio-Scaffolder 3.2, equipped with precision linear *X*-, *Y*-, and *Z*-axes driven by belt drives with iterative position correction. The motion system offers, in the *XY* plane, a nominal step width of 2 μm and a specified repetitive accuracy of ±10 μm. In our experimental methodology, following that of Dalton and coworkers,[11] the interfiber distance resolution was evaluated by printing a single line and

subsequently moving the stage laterally in small increments corresponding to the IFD to deposit a new parallel line. Given the small step sizes, consistent movement direction, and short travel distances involved, the effective positioning accuracy in this specific case is expected to be governed by the step width of the system (2 μm) rather than its specified repetitive accuracy (±10 μm), which applies primarily to larger or more complex movements.

The printhead consisted of a temperature-controlled stainless-steel cartridge with a 100 μm conic nozzle. The ink-filled cartridges were preconditioned at 25 °C for 2 hours before printing to ensure thermal and material stability.

During printing, a positive voltage was applied to the collector plate while the printhead remained grounded. The internal software manages processing parameters such as pressure, height, temperature, and printing speed. All printing parameters were optimized to ensure stable extrusion and consistent fiber morphology.

Scaffold design and execution. G-Code commands were initially prepared using CAD fusion software from Aerotech Inc. Modifications of the code for a proper interface with the GESIM Bio-Scaffolder router were manually done.

Substrate and melt electrowriting protocol. The MEW procedure involved depositing fibers onto ITO glass substrates (10 Ω sq.$^{-1}$ surface resistivity), carefully cleaned with soap, acetone, and isopropanol, followed by ozone treatment. The ITO was electrically connected to the collector with copper tape. All experiments were performed on identical ITO-coated glass collectors to ensure consistent charge dissipation and to isolate the effect of UV curing intensity on printing resolution. A consistent separation between the nozzle and substrate was maintained throughout (2 mm from the ITO glass), with a minor increase in nozzle height after each layer to accommodate the growing structure. During deposition, UV light reached the deposited fibers, initiating liquid crystal elastomer (LCE) crosslinking. An EXFO OmniCure S2000 UV lamp (Gentec, Nivelles, Belgium) equipped with a bandpass filter (320–390 nm) was used to irradiate the printing area directly from above. UV intensities of up to 15 mW cm^{-2} were applied at the sample plane.

Post-printing protocol. After final layer deposition, the scaffold is kept in a two-step UV irradiation process, first under ambient conditions and then intensified under vacuum to ensure thorough crosslinking.

SEM analysis. SEM analysis was launched on the Inspect F50 (FEI) at 10 kV with a coating of 10 nm Palladium under high vacuum conditions.

Image measurement. The straight-line selection tool of Fiji software was used to measure IFD and fiber diameters and crop the SEM images. Measurements were taken at 10 random regions within the SEM image, and mean values were calculated.

POM analysis. The LCE scaffolds were evaluated under a Nikon Eclipse 80i POM.

Thermoactuation experiment. The printed grid scaffold was placed in a homemade oven with a circular opening (30 mm diameter). The sample was fixed inside the oven cavity, and the temperature was monitored using a thermocouple placed close to the sample. The thermo-actuation process was observed and recorded using an Euromex magnifier.

FTIR analyses. FTIR measurements were launched on a Varian 670-IR infrared spectrometer at ambient temperature.

Author contributions

Mehrzad Javadzadeh: conceptualization, methodology, investigation, writing (original draft), writing (review and editing); María Férnandez-Melero: investigation, writing (review and editing); Jesús del Barrio: conceptualization, methodology, investigation, writing (review and editing); Carlos Sánchez-Somolinos: conceptualization, methodology, investigation, writing (original draft), writing (review and editing).

Conflicts of interest

There are no conflicts to declare.

Data availability

The data that support the findings of this study are available from the corresponding author upon reasonable request.

Supplementary information (SI) is available. See DOI: https://doi.org/10.1039/d5ma01174d.

Acknowledgements

The described research is part of the project PRIME. This project received funding from the European Union's Horizon 2020 research and innovation program under Grant Agreement No. 829010 (PRIME). Funding had also been received from the Spanish "Ministerio de Ciencia, Innovación y Universidades (MCIU)" MICIU/AEI/10.13039/501100011033, grants PID2020-118485RB-I00 and CEX2023-001286-S, and through grant CNS2022-135887 funded by MICIU/AEI/10.13039/501100011033 and by the European Union NextGenerationEU/PRTR, Gobierno de Aragón project PROY_E28_24, FEDER (EU) and Fondo Social Europeo (DGA E15_20R and E47_20R). This research was also supported by CIBER – Consorcio Centro de Investigación Biomédica en Red – (CB06/01/00263), Instituto de Salud Carlos III, Ministerio de Ciencia e Innovación. M. F.M. acknowledges Gobierno de Aragón for a predoctoral fellowship (2023–2027). The authors would like to acknowledge the use of the Laboratorio de Microscopias Avanzadas and the Servicio General de Apoyo a la Investigación-SAI, Universidad de Zaragoza. C. S. S. acknowledges the FAB3D interdisciplinary platform (PTI-CSIC) for support. The authors acknowledge Rosa Isabel Merino, from INMA, for fruitful discussions on charge dissipation phenomena.

References

1 A. A. Issa, M. Al-Maadeed, A. S. Luyt, M. Mrlik and M. K. Hassan, *J. Appl. Polym. Sci.*, 2016, **133**(26), 43594.
2 T. Jungst, W. Smolan, K. Schacht, T. Scheibel and J. Groll, *Chem. Rev.*, 2016, **116**, 1496–1539.
3 J. E. Smay, G. M. Gratson, R. F. Shepherd, J. Cesarano and J. A. Lewis, *Adv. Mater.*, 2002, **14**, 1279–1283.
4 I. Zein, D. W. Hutmacher, K. C. Tan and S. H. Teoh, *Biomaterials*, 2002, **23**, 1169–1185.
5 T. D. Brown, P. D. Dalton and D. W. Hutmacher, *Adv. Mater.*, 2011, **23**, 5651–5657.
6 A. Hrynevich, B. Ş. Elçi, J. N. Haigh, R. McMaster, A. Youssef, C. Blum, T. Blunk, G. Hochleitner, J. Groll and P. D. Dalton, *Small*, 2018, **14**, 1800232.
7 F. Chen, G. Hochleitner, T. Woodfield, J. Groll, P. D. Dalton and B. G. Amsden, *Biomacromolecules*, 2016, **17**, 208–214.
8 E. Bakirci, N. Schaefer, O. Dahri, A. Hrynevich, P. Strissel, R. Strick, P. D. Dalton and C. Villmann, *Adv. Biosyst.*, 2020, **4**, 2000077.
9 F. Tourlomousis, H. Ding, D. M. Kalyon and R. C. Chang, *J. Manuf. Sci. Eng.*, 2017, **139**(8), 081004.
10 P. D. Dalton, *Curr. Opin. Biomed. Eng.*, 2017, **2**, 49–57.
11 J. Kim, E. Bakirci, K. L. O'Neill, A. Hrynevich and P. D. Dalton, *Macromol. Mater. Eng.*, 2021, **306**, 2000685.
12 H. Ding, K. Cao, F. Zhang, W. Boettcher and R. C. Chang, *Mater. Des.*, 2019, **178**, 107857.
13 K. Cao, F. Zhang, A. Zaeri, R. Zgeib and R. C. Chang, *Adv. Mater. Technol.*, 2021, **6**(7), 2100251.
14 H. Xu, S. Fujiwara, L. Du, I. Liashenko, S. Luposchainsky and P. D. Dalton, *Polymer*, 2024, **309**, 127466.
15 L. Du, L. Yang, H. Lu, L. Nie, Y. Sun, J. Gu, S. Fujiwara, S. Yagi, T. Xu and H. Xu, *Polymer*, 2024, **301**, 127028.
16 A. Minařík, A. Mráček and P. Dalton, *ChemRxiv*, 2024, preprint, DOI: 10.26434/chemrxiv-2024-4mst2.
17 M. Javadzadeh, J. del Barrio and C. Sánchez-Somolinos, *Adv. Mater.*, 2023, **35**, 2209244.
18 F. Gholami, L. Yue, M. Li, A. Jain, A. Mahmood, M. Fratarcangeli, R. Ramprasad and H. J. Qi, *Adv. Mater.*, 2024, **36**(46), 202408774.
19 M. López-Valdeolivas, D. Liu, D. J. Broer and C. Sánchez-Somolinos, *Macromol. Rapid Commun.*, 2018, **39**, 1700710.
20 T. D. Brown, P. D. Dalton and D. W. Hutmacher, *Prog. Polym. Sci.*, 2016, **56**, 116–166.
21 F. M. Wunner, P. Mieszczanek, O. Bas, S. Eggert, J. Maartens, P. D. Dalton, E. M. De-Juan-Pardo and D. W. Hutmacher, *Biofabrication*, 2019, **11**, 025004.
22 D. J. Broer and G. N. Mol, *Polym. Eng. Sci.*, 1991, **31**, 625–631.
23 A. Nguyen, T. C. Rhoades, R. D. Johnson and K. M. Miller, *Macromol. Chem. Phys.*, 2017, **218**(21), 1700337.
24 M. Zhang, F. Makhlooghiazad, U. Pal, M. Maleki, S. Kondou, G. A. Elia, C. Gerbaldi and M. Forsyth, *ACS Appl. Polym. Mater.*, 2024, **6**, 14469–14476.
25 A. Hrynevich, I. Liashenko and P. D. Dalton, *Adv. Mater. Technol.*, 2020, **5**, 2000772.